J Mol Model (2014) 20:2484
DOI 10.1007/s00894-014-2484-1

ORIGINAL PAPER

Density functional theory (DFT) study of the gas-phase decomposition of the $Cd[(^{i}Pr)_2PSSe]_2$ single-source precursor for the CVD of binary and ternary cadmium chalcogenides

Francis Opoku · Noah Kyame Asare-Donkor · Anthony A. Adimado

Received: 13 May 2014 / Accepted: 6 October 2014 / Published online: 23 October 2014

Abstract The chemistry of group II–VI semiconductors has spurred considerable interest in decomposition reaction mechanisms and has been exploited for various technological applications. In this work, computational chemistry was employed to investigate the possible gas-phase decomposition pathways of the mixed $Cd[(^{i}Pr)_2PSSe]_2$ single-source precursor for the chemical vapour deposition of cadmium chalcogenides as thin films. The geometries of the species involved were optimised by employing density functional theory at the MO6/LACVP* level. The results indicate that the steps that lead to CdS formation on the singlet potential energy surface are favoured kinetically over those that lead to CdSe and ternary $CdSe_xS_{1-x}$ formation. On the doublet PES, the steps that lead to CdSe formation are favoured kinetically over those that lead to CdS and $CdSe_xS_{1-x}$ formation. However, thermodynamically, the steps that lead to ternary $CdSe_xS_{1-x}$ formation are more favourable than those that lead to CdSe and CdS formation on both the singlet and the doublet PESs. Density functional theory calculations revealed that the first steps exhibit huge activation barriers, meaning that the thermodynamically favourable process takes a very long time to initiate.

Keywords Chalcogenides · Chemical vapour deposition · Single-source precursor · Gas phase · Potential energy surface · Density functional theory

F. Opoku · N. K. Asare-Donkor (✉) · A. A. Adimado
Department of Chemistry, Kwame Nkrumah University of Science and Technology, Kumasi, Ghana
e-mail: asaredonkor@yahoo.co.uk

F. Opoku
e-mail: ofrancis2010@gmail.com

A. A. Adimado
e-mail: tonyadimado@yahoo.co.uk

Introduction

Cadmium chalcogenides are interesting members of the II–VI semiconductor family due to their unique chemical and physical properties [1]. Cadmium selenide thin films are used in devices such as light-emitting diodes, lasers, holographic optical memories, photonic band-gap crystals, ultrafast photonic switches, and biomedical tags for fluoroimmunoassays, nanosensors, as well as in biological imaging [2]. Cadmium sulfide has potential applications in photochemical catalysis, solar cells and nonlinear optical materials [3], and can be used as a bioorganic detector of proteins [4] and DNA [5, 6].

Metal-containing thin films have traditionally been prepared by a number of techniques, which can be classified according to the film formation environment: electrolysis (e.g. electrolytical anodisation, electroplating), vacuum (vacuum evaporation, ion beam deposition, molecular beam epitaxy, ion implantation), plasma (sputtering deposition, ion plating), liquid phase (liquid-phase epitaxy), solid state (solid-state epitaxy) and chemical vapour (substrate chemical vapour conversion, chemical vapour deposition) [7]. Each of these techniques has its own advantages and limitations, so different techniques are used in the fabrication of metal-containing thin films for different applications. Chemical vapour deposition (CVD) methods have the attraction of being able to deposit relatively large amounts of materials at high growth rates and low cost [7]. CVD methods using single-source precursors possess some potential intrinsic advantages, such as improved air/moisture stability of the precursor, easy purification, a relatively low deposition temperature (excluding pre-reaction) and lower toxicity [7].

The use of toxic and highly volatile organometallic precursors such as metal alkyls, phosphines and hydrogen selenide has many disadvantages, such as unwanted side reactions, impurity incorporation and a high deposition temperature. Precursors in which the elements of a binary semiconductor

are within a single molecule are of considerable interest to those attempting to overcome such problems [8]. The use of single-source precursors for the synthesis of metal chalcogenide thin films has proven to be an efficient route to the deposition of high-purity materials at low cost.

Much of the early work in this area of research was performed on readily prepared phenyl derivatives [9]. However, precursors based on isopropyl derivatives are better for CVD applications due to their higher volatility than phenyl-substituted derivatives [10]. Isopropyl derivatives can also be used as single-source precursors for the deposition of metal chalcogenide thin films [11, 12].

Optimising the CVD conditions such that higher-purity materials are obtained at a higher growth rate requires knowledge of the corresponding deposition chemistry, which is obtained by performing specially designed experiments or/and modelling and simulation. Experiments provide the most reliable results, but experimental investigations carried out in situ are very demanding, expensive, and consume large amounts of material and time. Recent developments in the field of quantum chemical methods, particularly density functional theory (DFT), and the rapid advances that have occurred in software and hardware development mean that a consistent set of kinetic, thermodynamic and structural data can now be obtained. Thermodynamic and kinetic analysis is important for understanding and optimising the deposition conditions of selective growth processes.

Studies performed by Akhtar et al. [13] allow us to rationalise a mechanism for the gas-phase decomposition of the $Cd[(^{i}Pr)_2PSSe]_2$ single-source precursor (see Fig. 1 for the geometry of this precursor). In the work reported in this paper, several reaction mechanisms for the thermal decomposition of the $Cd[(^{i}Pr)_2PSSe]_2$ single-source precursor in the gas phase were explored using density functional theory at the MO6/LACVP* level, and possible mechanistic channels for the formation of a ternary phase were investigated. Gaining a knowledge of the thermal decomposition reactions that occur during the CVD of binary and ternary cadmium chalcogenides is important in relation to analysing the Gibbs free energies for the gas-phase processes. Multiple spin states were considered in the calculations, as a change of spin state can affect the molecular structure in terms of its bond lengths, angular distortions, and even the overall molecular geometry, which can influence whether a chemical decomposition reaction takes place [14].

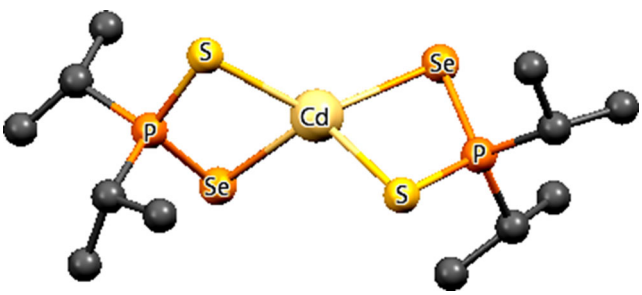

Fig. 1 Optimised geometry of the $Cd[(^{i}Pr)_2PSSe]_2$ single-source precursor

Details of the calculations performed

All calculations were carried out with the Spartan 10 v1.1.0 molecular modelling software [15] at the DFT MO6/LACVP* level of theory. The LACVP* basis set is a relativistic effective core potential developed by Dunning for first-row elements [16]. The Los Alamos ECP plus double zeta basis set developed by Wadt and Hay was used for the atoms Na–La, Hf–Bi [17–19]. The M06 functional has been tested against main-group ground- and excited-state energetics, and it has been applied to transition metals [20]. This functional has been used to study the noncovalent interactions, thermochemistry and kinetics of main-group and transition metals. It has found considerable use in relation to noncovalent interactions in organometallic and inorganometallic chemistry [20].

The starting geometries of the molecular systems were constructed using Spartan's graphical model builder and were minimised interactively using the Sybyl force field [21]. All geometries were fully optimised without any symmetry constraints. The normal mode of analysis was performed to verify the nature of the stationary points, and equilibrium geometries were characterised by the absence of imaginary frequencies.

The transition-state structures were located by performing the transition state geometry calculation at the DFT MO6/LACVP* level, fixing the breaking bonds at various lengths and optimising the remaining internal coordinates. The approximate stationary points located in this procedure were then fully optimised using the standard transition-state optimisation procedure in Spartan. The ChemDraw Ultra 12.0 graphical software was used to draw the energy profile and the Mercury 3.3 software was used to visualise the optimised structures. All of the computations were performed on Dell Precision T3400 workstation computers.

The rate constants were calculated using transition state theory for all elementary steps of the pathways discussed in this section. The unimolecular rate constant k_{uni} and equilibrium constants K_{eq} were computed using Eqs. 1 and 2, respectively, which were derived from transition state theory [22, 23] assuming that the transmission coefficient κ is equal to 1:

$$k_{\text{uni}} = \left(\frac{\kappa k_{\text{B}} T}{h}\right) \exp - \left(\frac{\Delta G^{\ddagger}}{RT}\right) \tag{1}$$

$$k_{\text{eq}} = \exp(-\Delta G^{\text{o}}/RT), \tag{2}$$

where $\Delta G^{\ddagger}$ is the Gibbs free energy change between the transition state and the reactant, ΔG^{o} is the Gibbs free energy change between the product and the reactant, and k_B and h are the Boltzmann and Planck constants, respectively.

The recombination rate constants (k_{rec}) were obtained by dividing the unimolecular rate constants (k_{uni}) by the equilibrium constants (k_{eq}).

Mechanistic considerations

A number of different thermal decomposition pathways as suggested by Akhtar et al. [13] were investigated for the $Cd[(^{i}Pr)_2PSSe]_2$ single-source precursor, and their corresponding reaction free energies ΔG^{o} were calculated at T= 800 K (Schemes 1, 2 and 3). The first two mechanisms considered (1, 2) involved the initial loss of an isopropyl radical to form **1a/d** on the doublet potential energy surface (PES). The next step is the loss of either $SP(^{i}Pr)$ or $SeP(^{i}Pr)$ from **1a/d** to form **1b/d** or **2b/d** on the doublet PES. The **1b/d** and **2b/d** intermediates further decompose to form $(^{i}Pr)_2PSSe$-Cd-Se (**1c/s**) and $(^{i}Pr)_2PSSe$-Cd-S (**2c/s**) on the singlet PES, which is followed by the decomposition of **1c/s** to give CdSe (**1d/s**) or $CdSe_xS_{1-x}$ (**1dt/s**), and **2c/s** to give CdS (**2d/s**) or $CdSe_xS_{1-x}$ (**2dt/s**) on the singlet PES. In the second set of possible mechanisms (3, 4) that was studied, the initial step involved the loss of an $[SeSP(^{i}Pr)_2]^{-}$ anion to form the intermediate $(^{i}Pr)_2PSSe$-Cd (**3a/d**) on the doublet PES. The subsequent step could be the loss of CdSe (**3b/s**), CdS (**4b/s**), or $CdSe_xS_{1-x}$ (**3bt/s**) from **3a/d** on the singlet PES. An alternative route (5, 6) was also investigated, involving the loss of an isopropyl radical to form $(^{i}Pr)PSSe$-Cd (**5b/d**) on the doublet

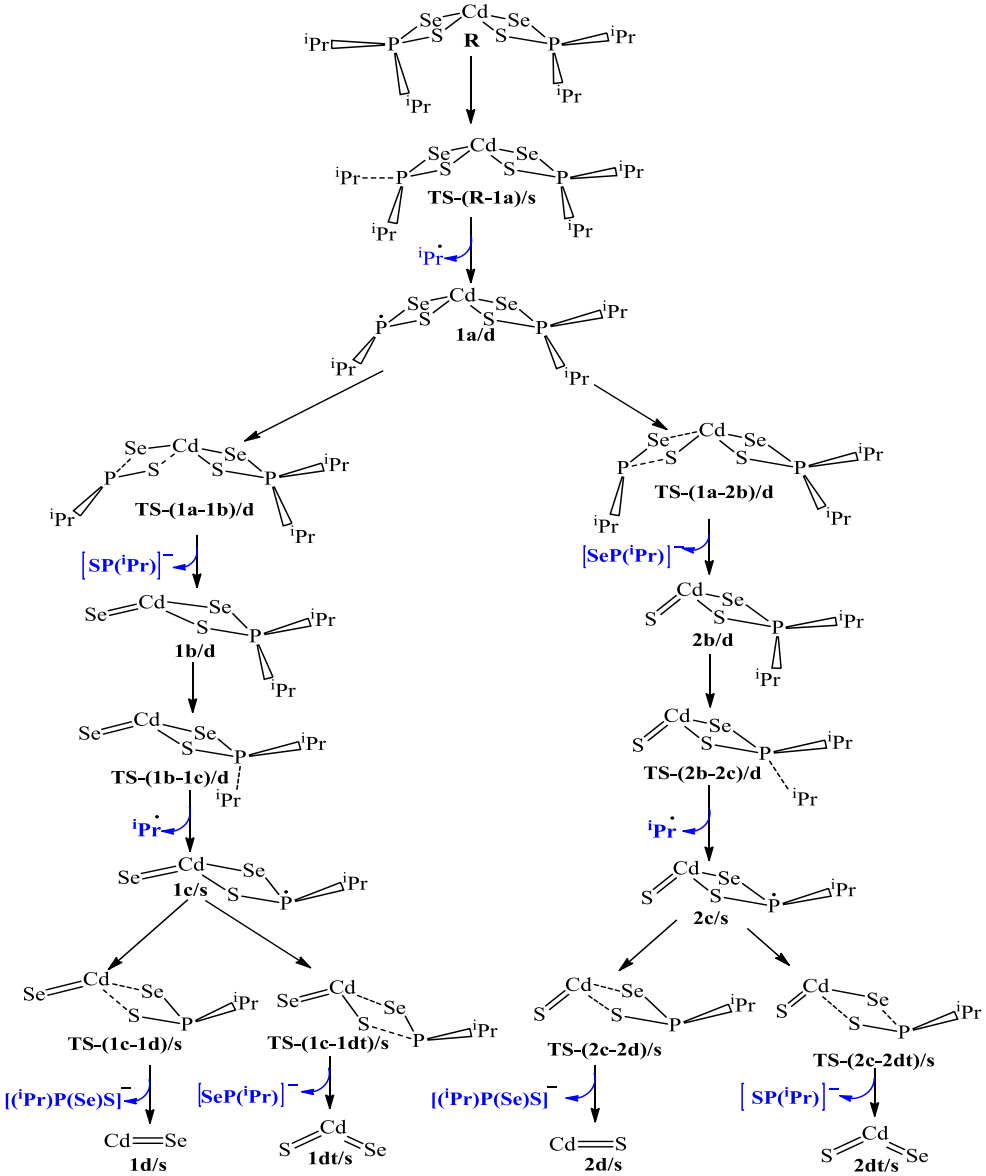

Scheme 1 Proposed gas-phase decomposition pathway (1, 2) of the $Cd[(^{i}Pr)_2PSSe]_2$ single-source precursor

Scheme 2 Proposed gas-phase decomposition pathway (3, 4) of the $Cd[(^iPr)_2PSSe]_2$ single-source precursor

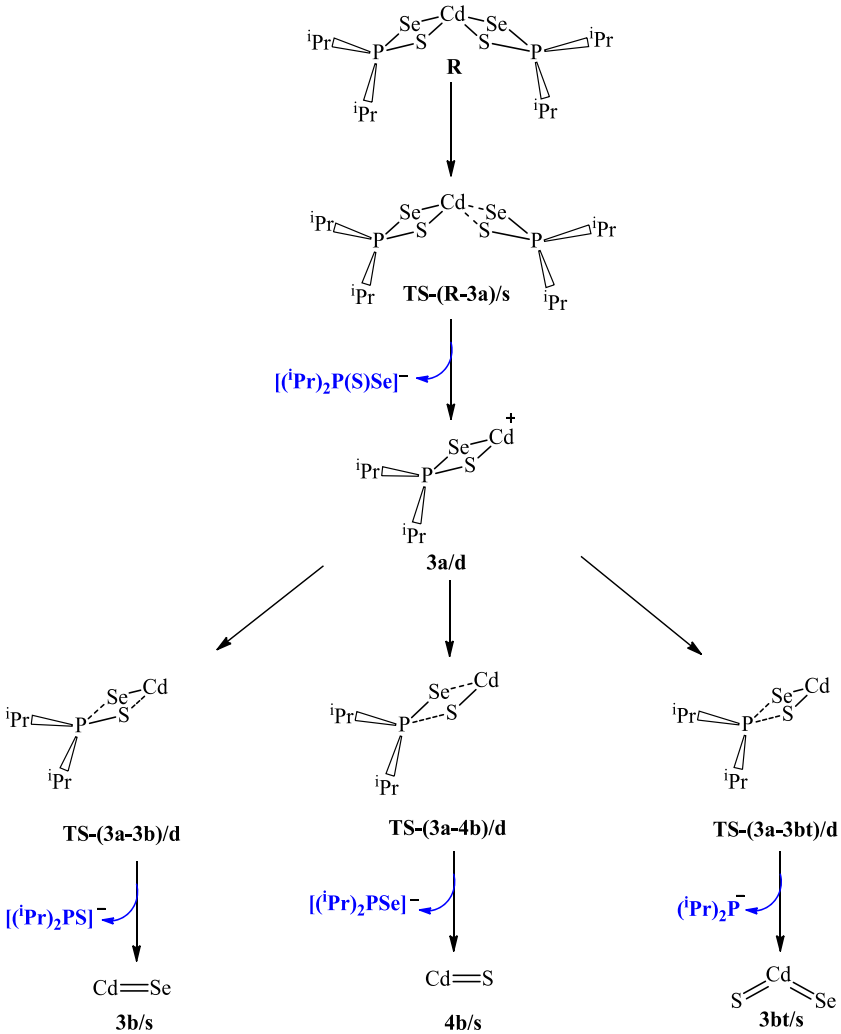

PES, and then the decomposition of **5b** to give CdSe (**5c/s**), CdS (**6c/s**) or $CdSe_xS_{1-x}$ (**5ct/s**) on the singlet PES.

Results and discussion

Optimised geometry of the $Cd[(^iPr)_2PSSe]_2$ single-source precursor

Table 1 shows some bond lengths and angles for the optimised geometry of the $Cd[(^iPr)_2PSSe]_2$ complex. To the best of our knowledge, there are no reports of the use of the $Cd[(^iPr)_2PSSe]_2$ complex as a single-source precursor for the deposition of cadmium chalcogenide thin films. Cadmium has a distorted tetrahedral geometry with ligand bond angles of 83.45 and 83.30°: these angles are smaller than the perfect tetrahedral angle. The two sulfur and two selenium atoms are located at the corners of the tetrahedron. Density functional theory (DFT) geometry optimisation of the $Cd[(^iPr)_2PSSe]_2$ precursor on the potential energy surface (PES) yields an average bond length of 2.51 Å (Cd–S), which is shorter than the length of the Cd–Se bond (2.54 Å) by 0.03 Å, suggesting that both Cd–S and Cd–Se fragments are likely to survive in the working temperature range of CVD.

Overall decomposition of the $Cd[(^iPr)_2PSSe]_2$ single-source precursor

Experimental and theoretical studies on the thermolysis of the $Pb[(C_6H_5)_2PSSe]_2$ single-source precursor have proposed two possible reaction pathways—PbSe and PbS abstraction as the final products in the decomposition of the $Pb[(C_6H_5)_2PSSe]_2$ precursor [13]. The cited study concludes that density functional theory calculations of the decomposition of the complex indicate that thermodynamic factors dominate over kinetic ones in terms of their influence on the material formed. By analogy, the same decomposition reactions were constructed for the $Cd[(^iPr)_2PSSe]_2$ single-source precursor, as shown in Schemes 1, 2 and 3. However, for pathways **1dt**, **2dt**, **3bt** and **5ct**, bond cleavage to form ternary cadmium chalcogenides has not been reported. Results for thermodynamic and kinetic parameters as well as the optimised structures of the main stationary points

Scheme 3 Proposed gas-phase decomposition pathway (5, 6) of the $Cd[(^iPr)_2PSSe]_2$ single-source precursor

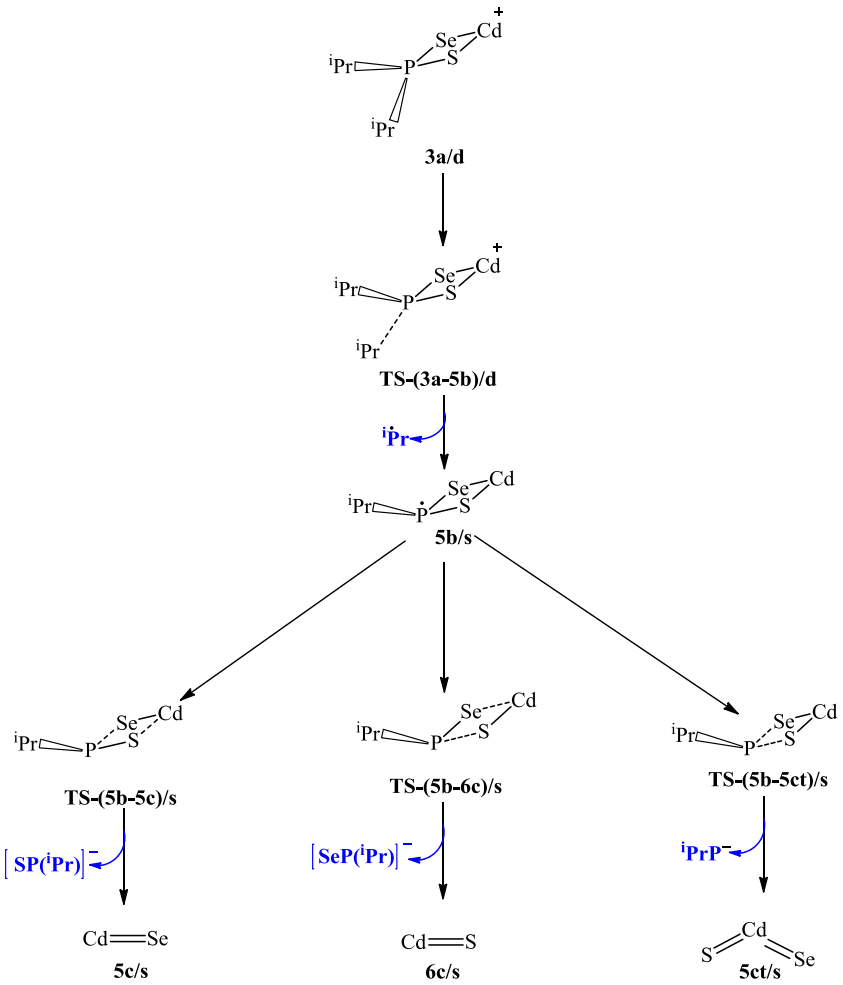

(reactants, transition states, intermediates and products) involved in the decomposition pathway (1, 2) are reported in Fig. 2. The optimised structures of reactants, intermediates, transition states and products for the gas-phase decomposition of the $Cd[(^iPr)_2PSSe]_2$ precursor using density functional theory (DFT) at the MO6/6-31G* level are given in Figs. 3, 4 and 5. DFT optimisation of the $Cd[(^iPr)_2PSSe]_2$ precursor shows that $Cd[(^iPr)_2PSSe]_2$ can have products with a singlet ground-state electronic structure and a doublet ground-state electronic structure.

Table 1 Selected bond lengths (Å) and bond angles (°) of the $Cd[(^iPr)_2PSSe]_2$ single-source precursor

Bond	Length (Å)	Bonds	Angle (°)
P–Se	2.20	Se–P–S	112.3
P–S	2.07	S–P–Se	112.2
S–P	2.07	Se–Cd–S	83.5
Se–P	2.20	S–Cd–Se	83.3
Cd–Se	2.81	Se–Cd–Se	124.9
Cd–S	2.51	S–Cd–S	119.6
Se–Cd	2.81	Se–Cd–S	116.4
S–Cd	2.51	S–Cd–Se	133.0

Data on the structural chemistry of the $Cd[(^iPr)_2PSSe]_2$ precursor are scarce. In particular, X-ray investigations and quantum-chemical models of the $Cd[(^iPr)_2PSSe]_2$ precursor have not been reported. Therefore, molecular and electronic structures as well as the ability of $[SeSPR_2]^-$ anions to coordinate to cadmium ions remain unexplored. Our calculations have revealed that the phosphorus atom in the $[SeSPPh_2]^-$ anion adopts a distorted tetrahedral geometry (Fig. 1). The P–Se and P–S bond lengths are intermediate between those of the corresponding single and double bonds.

The formation of the intermediate **1a/d** from the reactant **R** through the closed-shell singlet transition state **TS-(R-1a)/s** has an activation free-energy barrier of +76.72 kcal/mol^{-1} and is endergonic by 23.48 kcal/mol^{-1} on the doublet PES.

The doublet transition state (**TS-(1a-1b)/d** in Scheme 1) involved in the decomposition of **1a/d** to form the intermediate $(^iPr)_2$PSSe-Cd-Se (**1b/d**) has an activation free-energy barrier of +46.85 kcal/mol^{-1} and a reaction free energy of −21.94 kcal/mol^{-1} on the doublet PES. The **1a/d** intermediate can also decompose to form the intermediate $(^iPr)_2$PSSe-Cd-S

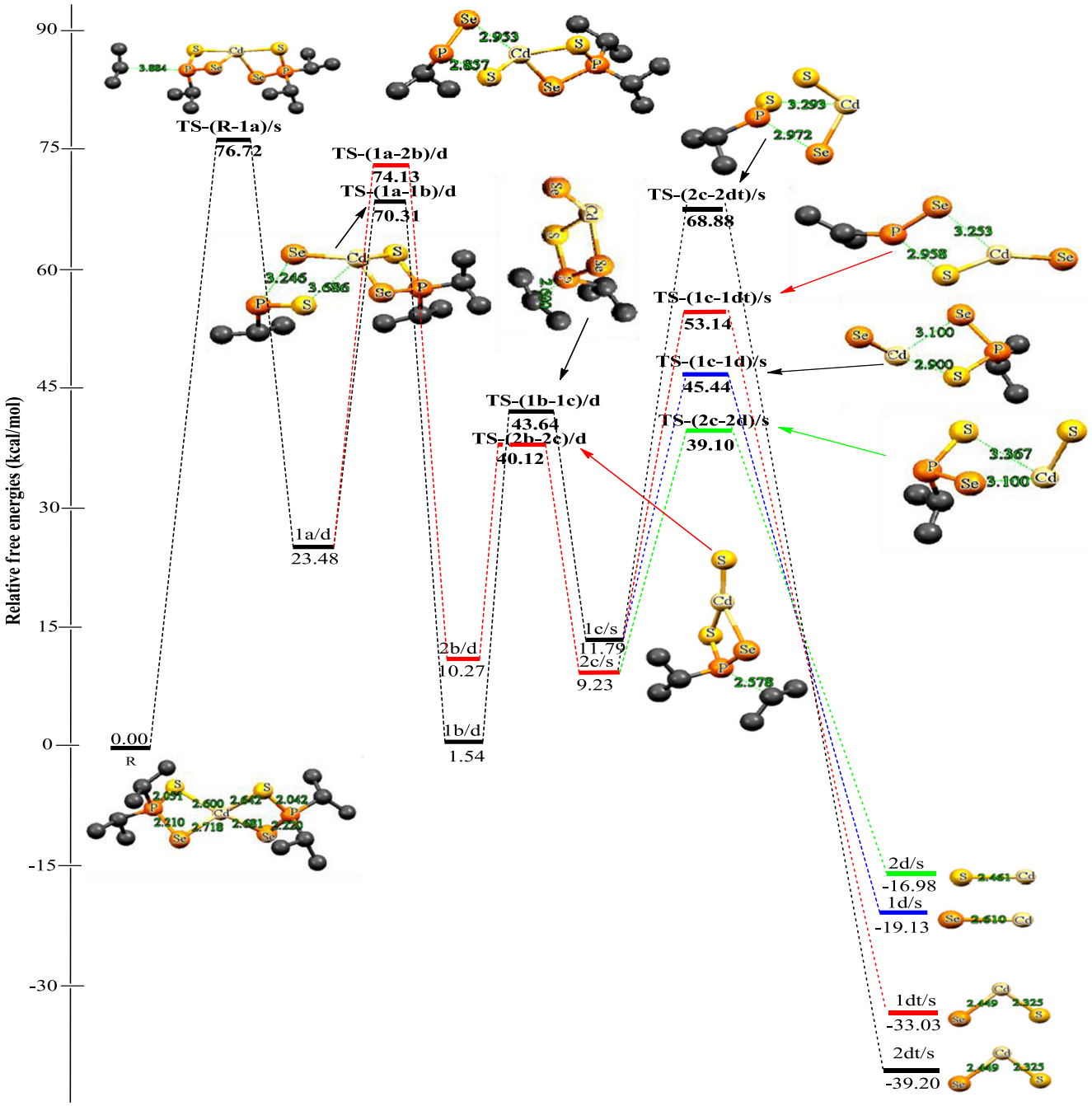

Fig. 2 Energetics of the unimolecular decomposition pathway (1, 2) at 800 K. The relative free energies are in kcal/mol^{-1} and bond distances are in Å

(**2b/d**) through the doublet transition state **TS-(1a-2b)/d** on the doublet PES. The activation free-energy barrier for this process is +50.65 kcal/mol^{-1}, and the reaction free energy is −13.21 kcal/mol^{-1}.

As shown in Fig. 2, if the reaction proceeds from the **1b/d** intermediate through the doublet transition state **TS-(1b-1c)/d** to form the intermediate (^{i}Pr)PSSe-Cd-Se (**1c/s**) on the singlet PES, the activation free-energy barrier is +42.10 kcal/mol^{-1}. Because the (^{i}Pr)PSSe-Cd-Se radical lies 10.25 kcal/mol^{-1} above **1b/d**, after isopropyl dissociation the system preferentially jumps to the singlet surface through internal conversion. The very unstable (^{i}Pr)PSSe-Cd-Se radical immediately dissociates, giving CdSe + (^{i}Pr)PSSe^{-} or the ternary $CdSe_xS_{1-x}$ + (^{i}Pr)PSe. If, on the other hand, it proceeds from the **2b/d** intermediate through the doublet transition state **TS-(2b-2c)/d** to form the intermediate (^{i}Pr)PSSe-Cd-S (**2c/s**) on the singlet PES; in this case, the activation free-energy barrier lies 29.85 kcal/mol^{-1} above **2c/s** and the reaction free energy is −1.04 kcal/mol^{-1}.

The singlet transition state (**TS-(1c-1d)/s** in Scheme 1) involved in the decomposition of the intermediate (^{i}Pr)PSSe-Cd-Se (**1c/s**) to form CdSe (**1d/s**) has an activation free-energy barrier of +33.65 kcal/mol^{-1} and a reaction free energy of

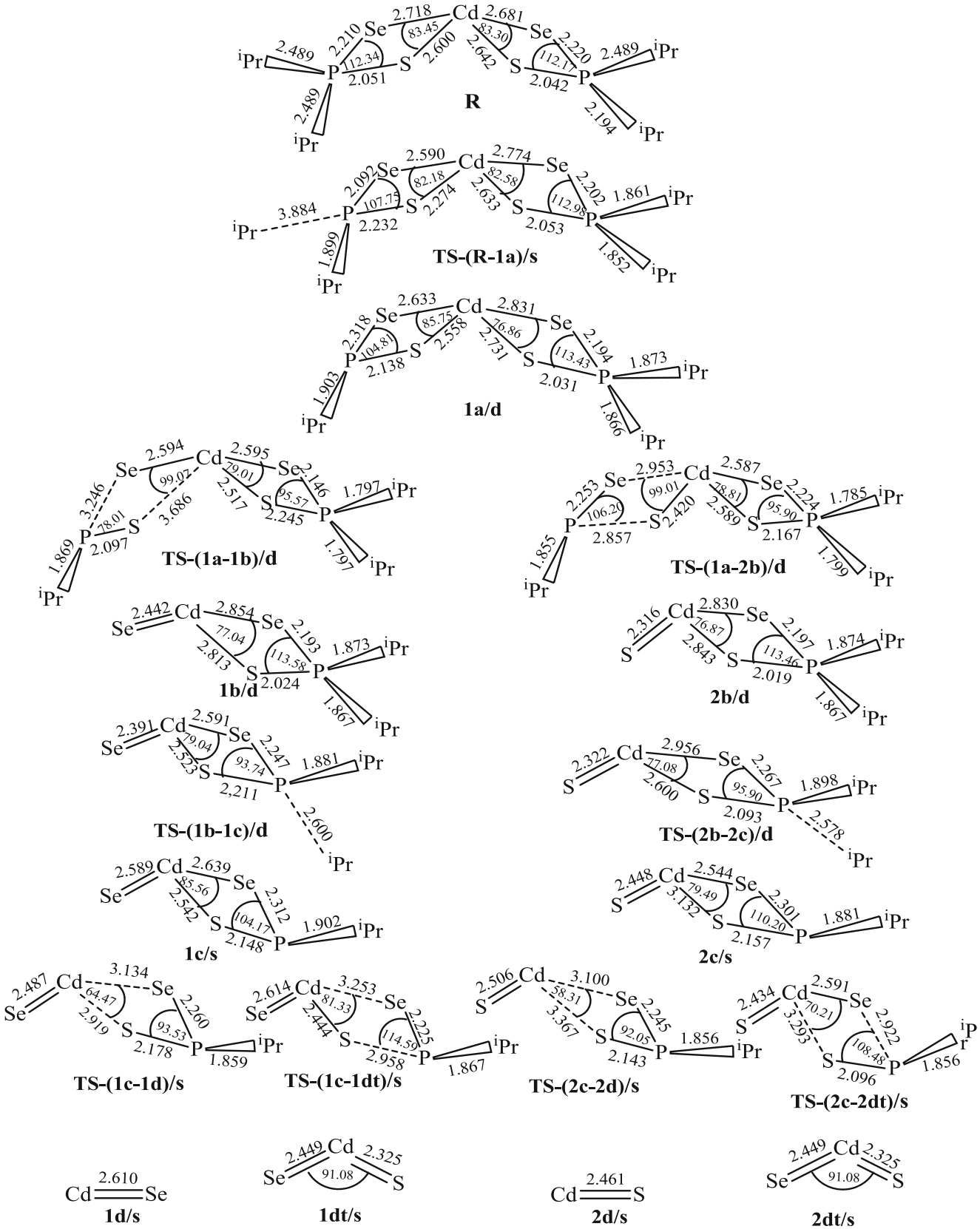

Fig. 3 Optimised geometrical parameters of the main stationary points involved in the unimolecular decomposition pathway (1, 2). Bond distances are in Å and bond angles are in degrees

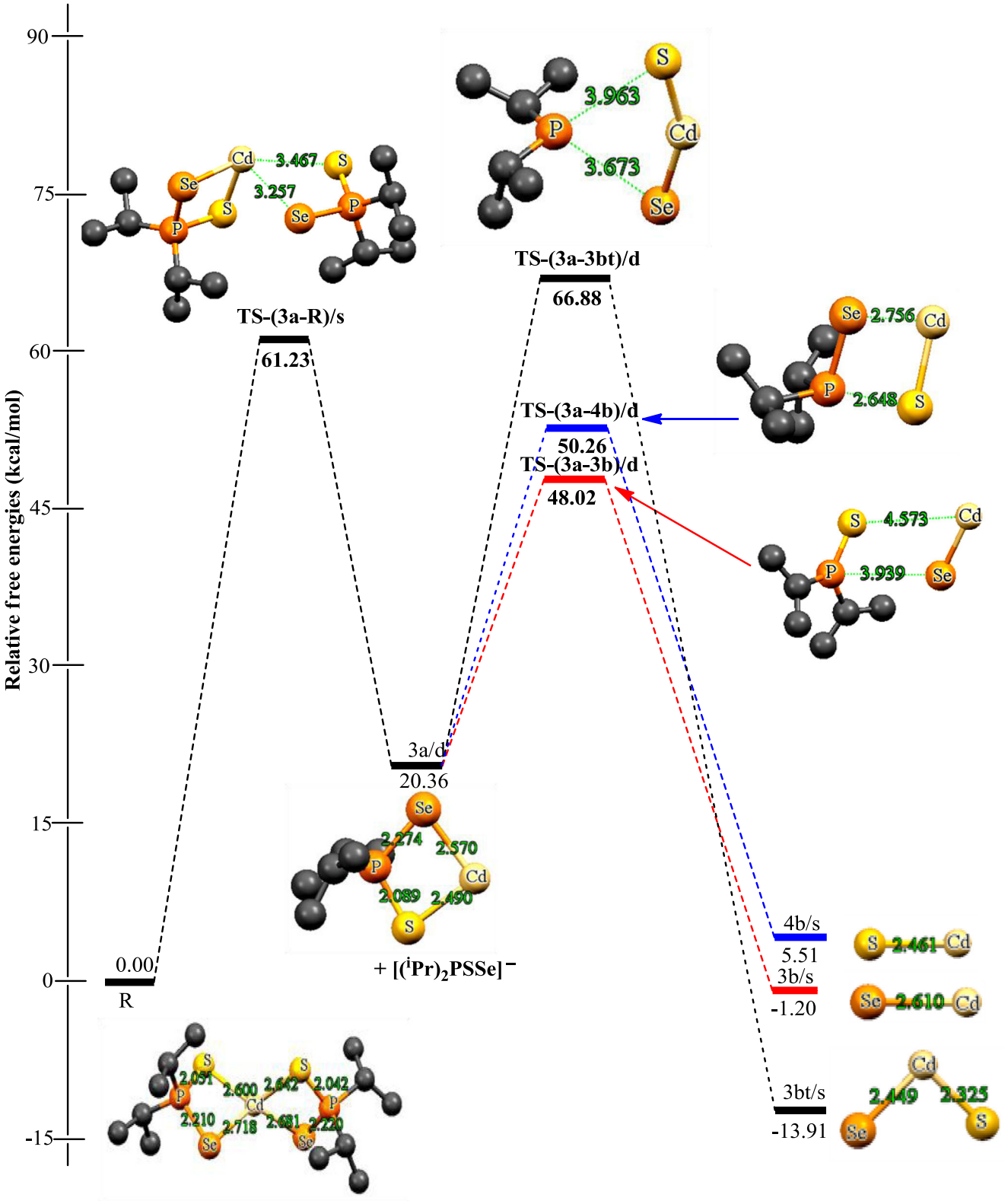

Fig. 4 Optimised geometrical parameters of the main stationary points involved in the unimolecular decomposition pathway (3, 4). Bond distances are in Å and bond angles are in degrees

−30.92 kcal/mol^{-1} on the singlet PES. The optimised geometry of **TS-(1c-1d)/s** reveals that the Cd–Se bond is elongated from 2.64 to 3.13 Å and the Cd–S bond lengthens from 2.54 to 2.92 Å. The formation of the ternary $CdSe_xS_{1-x}$ (**1dt/s**) along

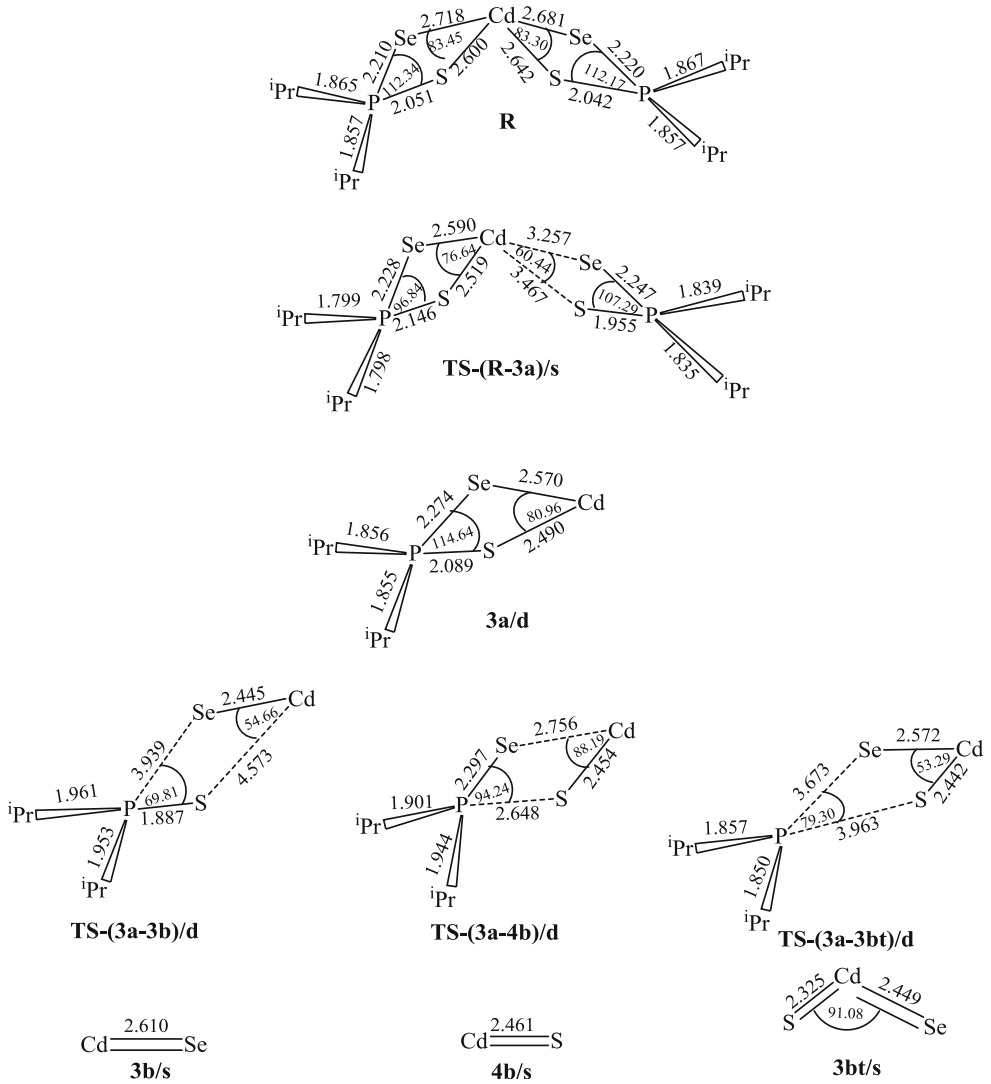

Fig. 5 Optimised geometrical parameters of the main stationary points involved in the unimolecular decomposition pathway (3, 4). Bond distances are in Å and bond angles are in degrees

the **1c/s** pathway through a singlet transition state (**TS-(1c-1dt)/s**) has an activation free-energy barrier of +41.35 kcal/mol^{-1} and is exergonic by 44.82 kcal/mol^{-1} on the singlet PES. The optimised geometry of **TS-(1c-1dt)/s** reveals that the Cd–Se bond elongates from 2.64 to 3.25 Å and the P–S bond lengthens from 2.15 to 2.96 Å.

Also, the decomposition of the intermediate (^{i}Pr)PSSe-Cd-S (**2c/s**) to form CdS (**2d/s**) through a singlet transition state (**TS-(2c-2d)/s**) has an activation free-energy barrier of + 29.87 kcal/mol^{-1} and a reaction free energy of −26.21 kcal/mol^{-1} on the singlet PES. The optimised geometry of **TS-(2c-2d)/s** reveals that the Cd–Se bond elongates from 2.54 to 3.10 Å and the Cd–S bond lengthens from 3.13 to 3.37 Å. The singlet transition state **TS-(2c-2dt)/s** along the **2c/s** pathway has a barrier of +59.65 kcal/mol^{-1} and is exergonic by 48.43 kcal/mol^{-1} on the singlet PES. The optimised geometry of **TS-(2c-2dt)/s** reveals that the Cd–S bond elongates from 3.13 to 3.29 Å and the P–Se bond lengthens from 2.30 to 2.97 Å. The calculations reveal that the activation barriers to the formation of CdSe (**1d/s**), CdS (**2d/s**) and ternary $CdSe_xS_{1-x}$ (**2dt/s** and **1dt/s**) are low, leading to thermodynamically favourable processes.

The results indicate that the **2d/s** elimination pathway will most likely interfere with CdSe formation because it is slightly more kinetically favourable than the **1d/s** elimination pathway. However, since the difference between these barriers is not very large (3.78 kcal/mol^{-1}), CdSe can also form. This means that CdS molecules can diffuse more easily across the surface, producing a smooth surface. The calculated rate constants also show that CdS formation is likely to occur very rapidly, with unimolecular and recombination rate constants of 3.47×10^{2} and 9.72×10^{14} s^{-1}, respectively. Any useful decomposition process should not only have a low barrier to the formation of intermediate(s) but also a low barrier to the subsequent decomposition of the intermediate(s) to form the

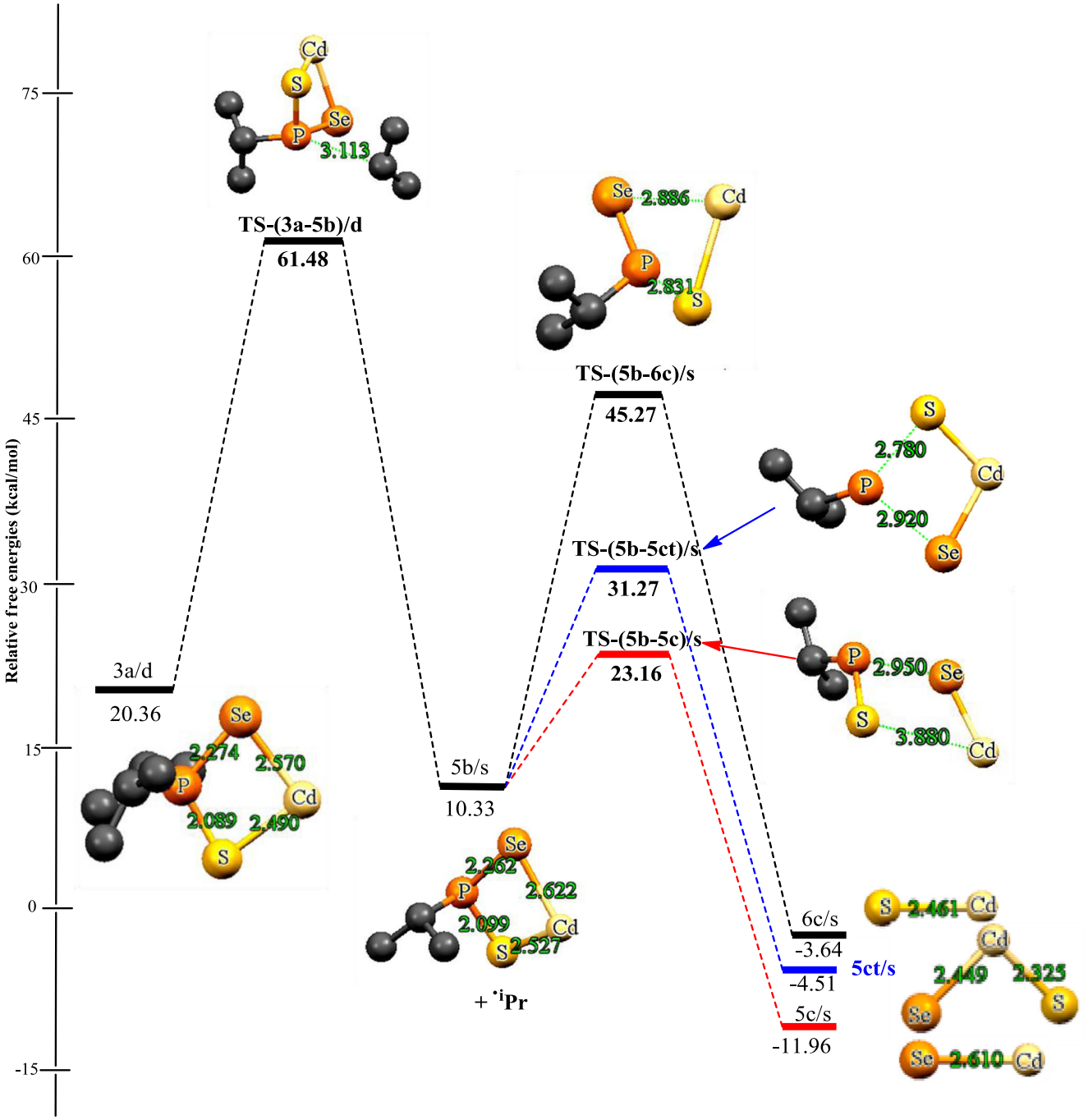

Fig. 6 Energetics of the unimolecular decomposition pathway (3, 4) at 800 K. The relative free energies are in kcal/mol^{-1} and bond distances are in Å

final product. Since the ternary $CdSe_xS_{1-x}$ is predicted to be very stable, its decomposition may not be feasible. Thus CdS may actually be the final product.

The relative free energies of the main stationary points involved in the gas-phase decomposition of the (^{i}Pr)$_2$PSSe-Cd intermediate are shown in Fig. 6. The full set of optimised structures for all of the systems reported herein is shown in Fig. 4. Density functional theory (DFT) optimisation of the reactant (^{i}Pr)$_2$PSSe-Cd shows that (^{i}Pr)$_2$PSSe-Cd can have a singlet ground-state electronic structure for the products and a doublet electronic ground-state structure for the intermediate, (^{i}Pr)PSSe-Cd.

The initial decomposition of the Cd[(^{i}Pr)$_2$PSSe]$_2$ precursor involves, as Scheme 2 shows, the elimination of the (^{i}Pr)$_2$PSSe$^-$ anion to form **3a/d** on the doublet PES, through the closed-shell singlet transition state **TS-(R-3a)/s**. The initial formation of (^{i}Pr)$_2$PSSe-Cd requires an energy of +20.36 kcal/mol^{-1} if it is produced via the decomposition of the Cd[(^{i}Pr)$_2$PSSe]$_2$ precursor, as shown in Fig. 6. The barrier to the conversion of Cd[(^{i}Pr)$_2$PSSe]$_2$ to **3a/d** is much larger than

Table 2 Calculated rate constants for the gas-phase decomposition of $Cd[(^iPr)_2PSSe]_2$ at 800 K

Reaction pathway	k_{uni} (s^{-1})	k_{eq}	k_{rec} (s^{-1})
1c → 1d	6.44×10^{1}	1.05×10^{14}	6.76×10^{15}
2c → 2d	3.47×10^{2}	2.80×10^{12}	9.72×10^{14}
1c → 1dt	5.07×10^{-2}	1.63×10^{24}	8.26×10^{22}
2c → 2dt	2.54×10^{-6}	5.44×10^{28}	1.38×10^{23}
3a → 3b	1.26×10^{5}	7.58×10^{6}	9.55×10^{11}
3a → 4b	3.10×10^{-1}	9.14×10^{-5}	2.83×10^{-5}
3a → 3bt	8.94×10^{-6}	1.57×10^{10}	1.40×10^{5}
5b → 5c	7.86×10^{6}	2.02×10^{3}	1.59×10^{10}
5b → 6c	7.16×10^{6}	4.65×10^{2}	3.33×10^{9}
5b → 5ct	4.78×10^{5}	5.85×10^{2}	2.80×10^{8}

the barriers to **3a→3b**, **3a→4b** and **3a→3bt**. The latter barrier is 61.23 kcal/mol^{-1} above the starting reactant. Therefore, **3a/d** is likely to have enough internal energy through internal conversion to overcome this barrier, forming **3b/d**, **4b/d** or **3bt/d**.

($^iPr)_2$PSSe-Cd (**3a/d**) decomposes to produce CdSe (**3b/s**) on the singlet PES through the doublet transition state **TS-(3a–3b)/d**. The energy required for this is −21.56 kcal/mol^{-1} relative to **3a/d**, with an activation free-energy barrier of +27.66 kcal/mol^{-1}. This means that the reaction is exergonic (energy is released). The lengths of the breaking Cd–S and P–Se bonds in **TS-(3a-3b)/d** are 4.57 and 3.94 Å, respectively. However, this decomposition pathway has the lowest activation free-energy barrier and will proceed very rapidly, with rate constants of 1.26×10^5 s^{-1} and 9.55×10^{11} s^{-1} (Table 2).

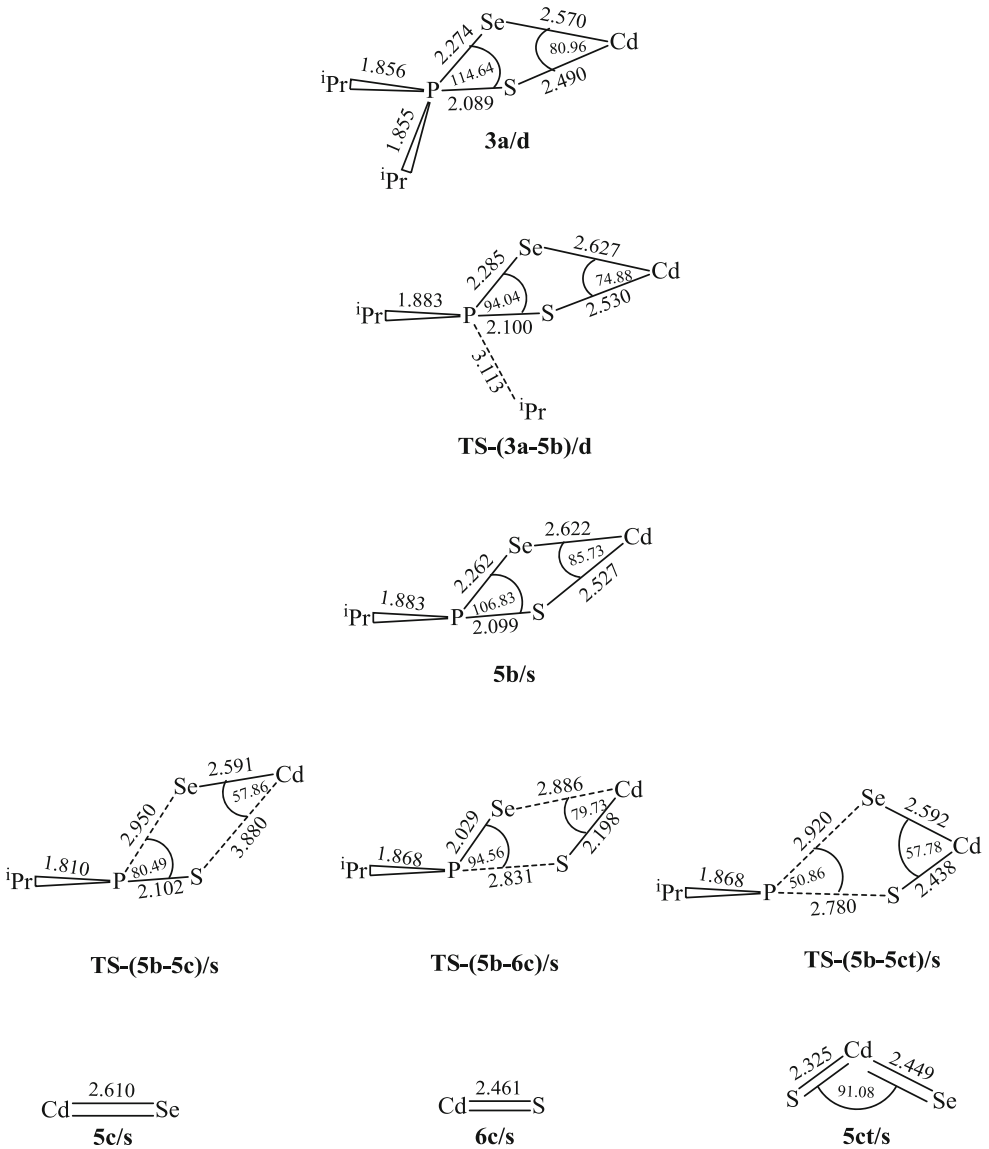

Fig. 7 Energetics of the unimolecular decomposition pathway (5, 6) at 800 K. The relative free energies are in kcal/mol^{-1} and bond distances are in Å

Table 3 Comparison of the S^2 values for some radicals and closed-shell transition states

Structure	(MO6/6-nd)
1b	0.7763
2b	0.7698
3a	0.7942
TS-(1a-1b)/d	1.3074[a]
TS-(1a-2b)/d	1.2060[a]
TS-(3a-3b)/d	0.7750
TS-(3a-4b)/d	0.7908
TS-(3a-3bt)/d	0.7883
TS-(3a-5b)/d	1.0376[a]

[a] Results for the unrestricted MO6 wave function

Following the first elimination, (^{i}Pr)$_2$PSSe-Cd (**3a/d**) can further decompose to form CdS (**4b/s**) on the singlet PES through Cd–Se and P–S elimination. A doublet transition state **TS-(3a-4b)/d** was found for this. In **TS-(3a-4b)/d**, the lengths of the Cd–Se and P–S bonds are 2.76 and 2.65 Å, respectively. The energy barrier to this process is 29.90 kcal/mol^{-1} above **3a/d**, while the relative energy is 14.85 kcal/mol^{-1} below **3a/d**.

The formation of the ternary $CdSe_xS_{1-x}$ (**3bt/s**) through the cleavage of the P–S and P–Se bonds in **3a/d** on the singlet PES via the doublet transition state **TS-(3a-3bt)/d** with a barrier of +46.52 kcal/mol^{-1} is a low-energy path that lies 34.27 kcal/mol^{-1} below **3a/d**. The energy barrier of this pathway does not favour this process, especially at the working temperature. In **TS-(3a-3bt)/d**, the lengths of the P–Se and P–S bonds are 3.67 and 3.96 Å, respectively.

The reaction mechanisms involved in the thermal decomposition of the intermediate (^{i}Pr)$_2$PSSe-Cd in the gas phase were studied by considering the energetics of the reactants, intermediates, transition states and products (Scheme 3). Figure 7 show the relative free energies of the main stationary points involved in the decomposition of the intermediate (^{i}Pr)PSSe-Cd and some of the optimised structures on the singlet and doublet PESs.

The decomposition of **3a/d** was further explored by first abstracting the isopropyl radical through a doublet transition state **TS-(3a-5b)/d** to form **5b/s** on the singlet PES. The activation free-energy barrier was found to be 41.12 kcal/mol^{-1} above **3a/d** and the reaction free energy was 10.03 kcal/mol^{-1} below **3a/d**.

(^{i}Pr)PSSe-Cd (**5b/s**) decomposes to produce CdSe (**5c/s**) on the singlet PES via the singlet transition state **TS-(5b-5c)/s**. The energy barrier to Cd–S and P–Se elimination through the singlet transition state **TS-(5b-5c)/s** is 12.83 kcal/mol^{-1} above **5b/s**, while the relative energy of **5c/s** is 22.29 kcal/mol^{-1} below **5b/s**, indicating that this reaction is exergonic. As shown in Fig. 7, the lengths of the Cd–S and P–Se bonds in **TS-(5b-5c)/s** are 3.88 and 2.95 Å, respectively.

The Cd–Se and P–S bonds in **5b/s** can also break to form stable CdS (**6c/s**) according to Scheme 3. The singlet transition state for this process was obtained as **TS-(3a-6c)/s**; its activation free-energy barrier is 34.94 kcal/mol^{-1} above **5b/s**. The relative reaction free energy is 13.97 kcal/mol^{-1} below **5b/s** on the singlet PES. In **TS-(3a-6c)/s**, the bond lengths of the Cd–Se and P–S bonds are 2.89 and 2.83 Å, respectively.

Similarly, **5b/s** decomposes to form the ternary $CdSe_xS_{1-x}$ (**5ct/s**) on the singlet PES through the singlet transition state **TS-(5b-5ct)/s**, with a barrier that is 20.94 kcal/mol^{-1} above **5b/s**. The low-energy path involves the cleavage of the P–Se and P–S bonds and the singlet transition state **TS-(5b-5ct)/s** with an energy of −14.84 kcal/mol^{-1}. In **TS-(5b-5ct)/s**, the lengths of the P–Se and P–S bonds are 2.92 and 2.78 Å, respectively.

The spin contamination S^2 of the Cd[(^{i}Pr)$_2$PSSe]$_2$ precursor was calculated using DFT. These calculations may also be relevant for transition states, since many contain partially broken bonds. All of the calculations included all core, valence, and unoccupied orbitals and utilised the 6-31G(d) basis set. Table 3 lists S^2 values for some radicals and transition states calculated at the MO6/6-31G(d) level of theory. All of the radicals and most of the closed-shell transition states discussed here have small values of S^2. The expectation values of the total spin operator are very close to the value expected for a pure doublet state (S^2=0.75), indicating that only the quartet is significantly admixed with the doublet state. This is expected, since S^2 is zero for the exact ground-state wave function and the correlated wave functions are closer to the exact wave function. For all of the unrestricted methods, S^2 tends to 1.0 as the bond dissociates. For a one-electron one-orbital system, if the orbitals are well separated and there is no interaction between the electrons, the unrestricted MO6 wave function contains an equal mixture of doublet (s=1/2) and quartet (s=/2) states, so the average value of S^2 should be 1.0. The UMO6 values of S^2 for **TS-(1a-1b)/d**, **TS-(1a-2b)/d** and **TS-(3a-5b)/d** are slightly larger than 1.0, indicating that the UMO6 wave function contains small contributions from

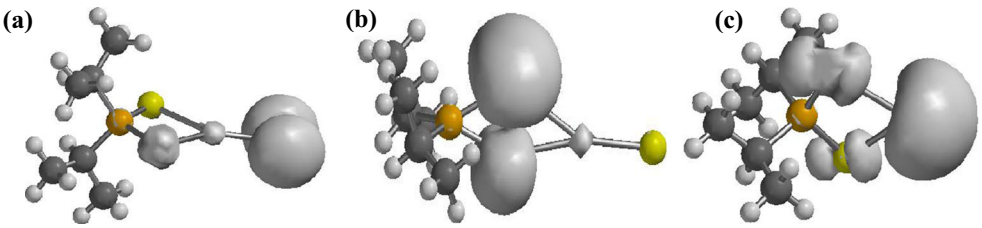

Fig. 8a–c Surfaces of spin density for the intermediates **a 1b**, **b 2b** and **c 3b** with σ-donor ligands. *Grey shapes* correspond to positive spin densities

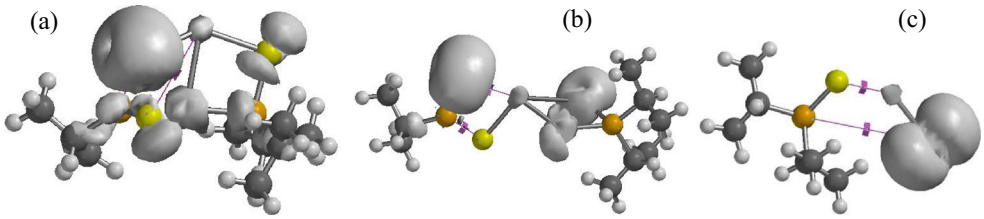

Fig. 9a–c Surfaces of spin density for **a TS(1a–1b)**, **b TS(1a–2b)** and **c TS(3a–3b)** with σ-donor ligands. *Grey shapes* correspond to positive spin densities

higher spin states ($s>1$). Density functionals such as UMO6 have much less spin contamination, probably because of admixture with DFT exchange. Even if the spin contamination calculated for the interacting system were twice as large as that for the noninteracting system, the spin contamination would still be relatively small, and it would be difficult to determine whether spin projection actually improves the calculations.

Spin density distribution maps depicting the $3N$-dimensional shapes of singly occupied molecular orbitals (SOMOs) are shown in Figs. 8, 9, and 10. The spin density distribution of the intermediate **2b** shows (a) a small spherical region of positive spin density at the metal centre, together with the spread of two-lobed positive spin density at the selenium in the nodal plane (Fig. 8a), (b) the p_z character of the spin density and the spin density displacement for the selenium atom in the nodal plane, and (c) no spin density at the bridging sulfur donor and phosphorus atom. The spin density distribution of the intermediate **2b** shows (a) a nicely cubic spin density at the metal centre (Fig. 8b), (b) positive spin density throughout the bridging Se and S ligands, and (c) no spin density at the selenium in the nodal plane. The spin density distribution of the intermediate **3a** shows (a) a large oval-shaped region of positive spin density at the metal centre, (b) a two-lobed orbital shape centred at the bridging selenium and the donar sulfur atom (Fig. 8c), and (c) no spin density at the phosphorus atom. Figure 9a shows (a) positive spin density throughout the plane of the phosphinite unit as well as (b) a two-lobed orbital shape centred on the bridging S-donor atom and a pear-shaped region of positive spin density at the donar Se atom. Figure 9b presents (a) a small region of spin density at the metal centre, (b) the existence of pear-shaped regions of positive spin density at the donor Se atom and a two-lobed orbital shape centred on the bridging S-donor atom, and (c) no spin density at the phosphorus and the donor S atom. Figure 9c reveals (a) a small region of positive spin density at the metal centre and a two-lobed orbital shape centred at the bridging donor Se atom as well as (b) no spin density at the phosphorus and the donor S atom. Figure 10a–c shows (a) a small region of positive spin density at the metal centre together with the spread of a two-lobed orbital shape centred on the bridging sulfur donor atom and a positive spin density at the selenium atom, as well as (b) no spin density at the phosphorus atom. Figure 10c also shows a two-lobed orbital shape centred on the phosphorus and the carbon atom. The metal *d* orbitals carry some positive spin density due to the polarisation of the electron pair in a low-lying bonding molecular orbital centred mainly on the ligands for all density surfaces except Fig. 8c. For the intermediate **3b**, the unpaired electrons at the metal atom are strongly localised, and the spin density at the metal atom is greater than the number of unpaired electrons due to spin polarisation of the bonding electron pairs. We found that the importance of the spin density at a given atomic orbital due to spin polarisation is roughly proportional to the number of unpaired electrons at the metal atom.

Conclusions

In this work, kinetic and thermodynamic parameters relating to the thermal decomposition behaviour of the mixed $Cd[(^{i}Pr)_2PSSe]_2$ single-source precursor were studied in the gas phase by performing DFT calculations at the MO6/6-31G* level. Several possible pathways were explored at T= 800 K. The following conclusions were drawn from the results presented above:

1. On the singlet PES, the **2d/s** dissociation of $(C_6H_5)P(Se)S$ from **2c/s** to form CdS has the lowest barrier. The barrier along this pathway is ~4 kcal/mol^{-1} lower than the **1d/s** elimination pathway, ~11 kcal/mol^{-1} lower than the **1dt/s**

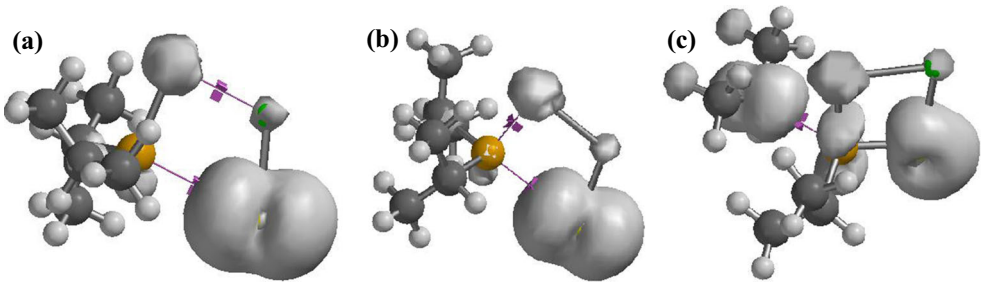

Fig. 10a–c Surfaces of spin density for **a TS(3a–4b)**, **b TS(3a–3bt)** and **c TS(3a–5b)** with σ-donor ligands. *Grey shapes* correspond to positive spin densities

elimination pathway and ~30 kcal/mol^{-1} lower than the **2d/s** elimination pathway (Fig. 2). Ternary $CdSeS_{1-x}$ formed by optimising **2c/s** is the most stable species on the reaction PES (~48 kcal/mol^{-1}, exergonic).

2. In terms of the kinetics, the most favourable pathway via ($^{i}Pr)_2PSSe$-Cd (**3a/d**) involves the dissociation of ($^{i}Pr)_2PS$ to form CdSe (**3b/s**). The barrier to this pathway is only about 2 kcal/mol^{-1} lower than that to the **4b/s** dissociation pathway and ~19 kcal/mol^{-1} lower than that to the **3bt/s** dissociation pathway. Ternary $CdSe_xS_{1-x}$ (**3bt/s**) formed by optimising **3a/d** is the most stable species on the reaction PES (~14 kcal/mol^{-1}, exergonic). Thermodynamically speaking, the most favourable pathway is the **3bt/s** dissociation pathway, with a rate constant of 1.57×10^{10} s^{-1}.
3. In terms of the kinetics, the **5c/s** dissociation pathway to form ternary CdSe is slightly more favourable than the **6c/s** and **5ct/s** dissociation pathways. The barrier to this pathway is about 22 kcal/mol^{-1} lower than that of the **6c/s** dissociation pathway and about 8 kcal/mol^{-1} lower than that of the **5ct/s** dissociation pathway. In terms of equilibrium thermodynamics, **5c/s**, formed during the optimisation of **5b/s**, is the most stable species on the reaction PES (~12 kcal/mol^{-1}, exergonic). The rate constant along this pathway is 1.57×10^{10} s^{-1}.
4. In summary, spin contamination occurs when a system's wave function or density incorporates character from higher spin states.
5. A systematic analysis of the shape of the spin density around the transition metal atom indicates that it can be spherical, cube-shaped, or have two lobes. A remarkable finding of this work is that, in specific cases, even if an unpaired electron residing on a metal atom is delocalised toward a ligand, a region of zero spin density appears along the metal–ligand bond.

Acknowledgments The authors are very grateful to the National Council for Tertiary Education (NTCE), Ghana, for a research grant under the Teaching and Learning Innovation Fund (TALIF-KNUSTR/3/005/2005). We are also grateful to the Computational Quantum Chemistry Laboratory at the Department of Chemistry, Kwame Nkrumah University of Science and Technology (KNUST), Kumasi, Ghana, for the use of their facilities for this work.

References

1. Xia Y, Yang P, Sun Y, Wu Y, Mayers B, Gates B, Yin Y, Kim F, Yan H (2003) One-dimensional nanostructures: synthesis, characterization and applications. Adv Mater 15:353–389
2. Bruchez M, Moronne M, Gin P, Weiss S, Alivisatos AP (1998) Quantum dot cell labeling. Science 281:2013–2016
3. Ma RM, Wei XL, Dai L, Huo HB, Qin GG (2007) Synthesis of CdS nanowire networks and their optical and electrical properties. Nanotechnology 18:1–5
4. Tan L, Liu L, Xie Q, Zhang Y, Yao S (2004) Fluorescence quenching of bovine serum albumin in reversed micelles by CdS nanoparticles. Anal Sci 20:441–444
5. Mahtab R, Rogers JP, Murphy CJ (1995) Protein-sized quantum dot luminescence can distinguish between "straight", "bent", and "kinked" oligonucleotides. J Am Chem Soc 117:9099–9100
6. Mahtab R, Rogers JP, Singleton CP, Murphy CJ (1996) Preferential adsorption of a "kinked" DNA to a neutral curved surface: comparisons to and implications for nonspecific DNA–protein interactions. J Am Chem Soc 118:7028–7032
7. Malik MA, Afzaal M, O'Brien P (2010) Precursor chemistry for main group elements in semiconducting materials. Chem Rev 110:4417–4446
8. Gleizes AN (2000) MOCVD of chalcogenides, pnictides, and heterometallic compounds from single-source molecule precursors. Chem Vap Depos 6:155–173
9. Bhattacharyya P, Novosad J, Phillips J, Slawin AMZ, Williams DJ, Woollins JD (1995) Bis(bidentate) complexes of imidobis(diphenylphosphinochalcogenides) [M{N(XPPh$_2$)$_2$–X, X'}$_2$] (X = S or Se; M = Ni, Pd or Pt). Dalton Trans 10:1607–1613
10. Afzaal M, Aucott SM, Crouch D, O'Brien P, Woollins JD, Park J-H (2002) Deposition of MSe (M = Cd, Zn) films by LP-MOCVD from novel single-source precursors M[(SePPh$_2$)$_2$N]$_2$. Chem Vap Depos 8:187
11. Kim S, Fisher B, Eisler H-J, Bawendi M (2003) Type-II quantum dots: CdTe/CdSe(core/shell) and CdSe/ZnTe(core/shell) heterostructures. J Am Chem Soc 125:11466–11667
12. Green M, Wakefield G, Dobson PJ (2003) A simple metalorganic route to organically passivated mercury telluride nanocrystals. J Mater Chem 13:1076
13. Akhtar J, Afzaal M, Vincent M, Burton N, Raftery J, Hillier I, O'Brien P (2011) Understanding the decomposition pathways of mixed sulphur/selenium lead phosphinato precursor explaining the formation of lead selenide. J Phys Chem C 115(34):16904–16909
14. Buchachenko AL (2000) Recent advances in spin chemistry. Pure Appl Chem 72:2243–2258
15. Wavefunction, Inc. (2010) Spartan. Wavefunction, Inc., Irvine
16. Dunning TH Jr, Hay PJ (1976) Gaussian basis sets for molecular calculations. In: Schaefer HF III (ed) Modern theoretical chemistry, vol 3. Plenum, New York, pp 1–28
17. Hay PJ, Wadt WR (1985) *Ab initio* effective core potentials for molecular calculations. Potentials for the transition metal atoms Sc to Hg. J Chem Phys 82:270–283
18. Hay PJ, Wadt WR (1985) *Ab initio* effective core potentials for molecular calculations. Potentials for K to Au including the outermost core orbitals. J Chem Phys 82:299–310
19. Wadt WR, Hay PJ (1985) *Ab initio* effective core potentials for molecular calculations. Potentials for main group elements Na to Bi. J Chem Phys 82:284–298
20. Zhao Y, Truhlar DG (2008) The M06 suite of density functionals for main group thermochemistry, thermochemical kinetics, noncovalent interactions, excited states, and transition elements: two new functionals and systematic testing of four M06-class functionals and 12 other functionals. Theor Chem Acc 120:215–241
21. Clark M, Cramer RD, Opdenbosch NV (1989) Validation of the general purpose Tripos 5.2 force field. J Comput Chem 10:982–1012
22. Benson SW (1960) The foundations of chemical kinetics. McGraw-Hill, New York
23. Glasstone S, Laidler KJ, Eyring H (1941) The theory of rate processes. McGraw-Hill, New York